

PFC/JA-92-32

**2D Full-Wave Simulation of
Ordinary Mode Reflectometry**

J.H. Irby, S. Horne, I.H. Hutchinson, and P.C. Stek

Plasma Fusion Center
Massachusetts Institute of Technology
Cambridge, MA 02139

November, 1992

Submitted to Plasma Physics and Controlled Fusion.

This work was supported by the U. S. Department of Energy Contract No. DE-AC02-78ET51013. Reproduction, translation, publication, use and disposal, in whole or in part by or for the United States government is permitted.

2D Full-Wave Simulation of Ordinary Mode Reflectometry

J.H. Irby, S. Horne, I.H. Hutchinson, and P.C. Stek

Plasma Fusion Center
Massachusetts Institute of Technology
Cambridge, Massachusetts, U.S.A.

Abstract

A 2D full-wave simulation of ordinary mode propagation has been developed in an effort to model effects seen in reflectometry experiments but not properly explained by 1D analysis. The geometric fall off of the fields, together with the effects of both refraction and diffraction, considerably modify the results obtained. The now commonly seen experimental observations of large amplitude and phase variations of the echo signal and occasional ramping of the phase can be explained by these 2D effects in the presence of fluctuations.

1. Introduction

During the last few years, reflectometry has proved to be a very useful diagnostic on several large toroidal plasma experiments (Simonet, 1985, Hubbard, 1987, Millot, 1990, Doyle, 1990). Not only have density profiles been measured, but large amounts of qualitative information have been gathered about fluctuations on these machines (TFR Group, 1985, Doyle, 1990, Hanson, 1990). One of the most intriguing aspects of these results, however, is the extreme apparent sensitivity of the signals to fluctuations. Large, rapid variations in return signal amplitude and phase are often seen (Hubbard, 1987, Hanson, 1989). In addition, several experiments report that the phase of the echo can in fact begin to ramp as a function of time, indicating a Doppler shift in the return signal relative to the transmitted one (Hanson, 1990, Bulanin, 1992, Sanchez, 1992). These effects cannot be easily explained with 1D analysis, but even very simplified 2D analysis in which the critical surface is modelled as a grating qualitatively explains some of the experimental results (Irby, 1990). The 2D, full-wave, cold plasma analysis presented in this paper not only explains some of the experimental observations, but also modifies what one might otherwise surmise about scattering, the response to fluctuations, and localization of the reflection to the critical surface, were only 1D results to be considered.

2. Code Description

We seek a solution to Maxwell's equations for the propagation of ordinary electromagnetic waves in a cold plasma. The first two equations of interest for this problem are

$$\nabla \times \mathbf{E} = -\frac{\partial \mathbf{B}}{\partial t}$$

$$\nabla \times \mathbf{B} = \mu_o \mathbf{J} + \epsilon_o \mu_o \frac{\partial \mathbf{E}}{\partial t} \quad (1)$$

where all plasma effects will be included in the response of the current density \mathbf{J} to the electric field \mathbf{E} (Hutchinson, 1987). Restricting ourselves now to two dimensions, with ordinary mode propagation in the x - y plane, and no gradients allowed in the z direction, a simplified set of equations result for the wave fields

$$\begin{aligned} \frac{\partial B_x}{\partial t} &= -\frac{\partial E_z}{\partial y} \\ \frac{\partial B_y}{\partial t} &= \frac{\partial E_z}{\partial x} \\ \mu_o \epsilon_o \frac{\partial E_z}{\partial t} &= -\mu_o J_z + \frac{\partial B_y}{\partial x} - \frac{\partial B_x}{\partial y} . \end{aligned} \quad (2)$$

The large static magnetic field normally found in plasma experiments has been assumed to be in the z direction and much larger than the wave fields, so that current flow is restricted to that direction.

In addition to the field equations, an equation describing the plasma response to the waves is needed. Normally, in the cold plasma approximation, all electrons are assumed to move harmonically in response to the wave fields oscillating at a frequency ω . In such cases, a Fourier analysis of the equation of motion for the electron leads to a simple expression for the current density

$$\mathbf{J} = \vec{\sigma} \cdot \mathbf{E} \quad (3)$$

where $\vec{\sigma}$ is the conductivity tensor and depends primarily on the electron density, magnetic field, and wave frequency (Hutchinson, 1987). However, since we wish to solve the time-dependent problem in which Doppler shifted waves are present at frequencies other than ω , we choose to solve the equation of motion for the electrons directly and write the equation

for the current density as

$$\frac{\partial J_z}{\partial t} = \epsilon_o \omega_p^2 E_z \quad (4)$$

where ω_p is the electron plasma frequency given by $\sqrt{n_e e^2 / \epsilon_o m_e}$, n_e is the electron density and a function of x and y only, e is the electron charge, and m_e the electron mass.

Note that, in our derivation of equations (2) and (4), we have assumed that the dielectric does not vary with time. On the other hand, in what follows, we will perturb the dielectric as a function of time in investigating fluctuations and density pulse propagation. All these perturbations will be done adiabatically, however, on time scales much longer than either the propagating wave period or the plasma response time.

Equations (2) and (4) together comprise a set of equations to be solved self-consistently. To do so, we adopt a finite-difference, time-domain scheme developed by Blaschak and Kriegsmann which is 2nd order in both space and time (Blaschak, 1987). The equations are solved on a rectangular grid, typically with a source of radiation near the left boundary, and the plasma critical surface near the right boundary. To insure stability of the code, several conditions must be met, including the Courant condition, $\delta x, \delta y \geq 2c\delta t$. Here δx , δy , and δt are the spatial and temporal increments used for the finite-difference time-dependent integration. In addition $\delta t \leq 2/\omega_p$ assures that the current density equation is integrated reliably. Finally, both δx and δy should be small compared to the vacuum wavelength of the propagating radiation. In all of the results quoted in this paper, $\delta t = \tau_o/20$, and $\delta x = \delta y = \lambda_o/10$, where τ_o is the source period, and λ_o is the source vacuum wavelength.

It is essential to emphasize the importance of radiative (vanishing reflection coefficient) boundary conditions for the problem discussed here. Without radiative boundaries, large standing wave patterns grow on

the grid and make it very difficult to draw even qualitative conclusions from the code results. Simply making the grid very large, as is sometimes done, will not work for this problem since one must also keep the grid spacing small compared to the vacuum wavelength if the code is to remain stable. Radiative boundary conditions are applied on the left, upper, and lower boundaries, while $E_z = 0$ is applied on the right boundary. The boundary on the right is well beyond the critical surface and is therefore well insulated from waves propagating to the critical surface from the left, so we can safely assume the fields are zero there. Radiative boundary conditions on the other three boundaries would imply that any waves propagating up to a boundary would continue through unimpeded and off the grid. Though we can not generate a perfect radiative boundary for an arbitrary incident wave, a method developed by Higdon (Higdon, 1986, Givoli, 1991), in which radiative conditions are found for plane waves incident at several specific angles, can be used. We adopt Higdon's second order expression in which the boundary is perfectly absorbing for two angles, α_1 and α_2 . The boundary condition at $x = 0$, for example, is given by

$$\left[\prod_{j=1}^2 (\cos \alpha_j \frac{\partial}{\partial t} - c \frac{\partial}{\partial x}) \right] E_z = 0 . \quad (5)$$

These conditions are sufficient to reduce the reflection coefficient at the boundaries to the 5% level, for all angles. Angles of 90 and 45 degrees were chosen for the left boundary, while angles of 45 and 22.5 degrees were used for the upper and lower boundaries.

The unperturbed plasma is modelled as

$$\frac{\omega_{p_0}^2}{\omega^2} = [\beta e^{-\psi}]^\gamma \quad (6)$$

where

$$\psi = \left[\frac{x - x_o}{w} \right]^2 + \left[\frac{y - y_o}{\kappa w} \right]^2. \quad (7)$$

ψ represents an elliptical surface with elongation κ on which the density is a constant. The plasma center is determined by x_o and y_o , while w and κ determine the relative scaling of the density in the x and y directions, and γ allows the density gradient to be scaled without changing the location of the critical surface. The critical surface may be scanned toward and away from the plasma center by adjusting β . Typical values for the above parameters were $\beta = 2.7183$, $\gamma = 1$, $x_o = 18.75\lambda_o$, $y_o = 0$, $w = 7.5\lambda_o$, and $\kappa = 4$.

Finally, waveguides and horns are modelled by setting up $E_z = 0$ boundary conditions inside the computational grid. Referring to Figure (1), the upper structure contains the transmitting horn and guide, the lower the receiving horn and guide. Note that the upper waveguide is closed on its left boundary. We insure in this way that all power generated in the guide propagates to the right and does not couple to the rear of the receiving guide. The receiving guide is left open so that standing waves will not be generated. Doing so is equivalent to having a well terminated detector at the end of the guide. The received power is monitored by recording, as a function of time, the signal at a grid point located near the left end of this guide at $x = \lambda_o$ and $y = -1.1\lambda_o$. In addition, as will be discussed below, several other grid points near the left boundary are monitored. Power is added to the system by sinusoidally driving current at the frequency ω at a grid point located near the left end of the upper waveguide. The current is allowed to rise slowly, over a four cycle period of time, since a rapid turn-on results in the generation of high frequency field components. To the left of this source, and filling

the source guide to its left boundary, is an absorber. The absorber damps waves that would normally re-enter the source waveguide after reflecting off of the plasma. In cases where the critical surface is very close to the horns, these waves can actually be detected at the receiving horn after a second reflection from the plasma, and they can therefore complicate the analysis. In the cases discussed in this paper, the critical surface was kept well away from the horns, reducing the need for the absorber.

3. General Features of the Solution

Referring again to Figure (1), power leaving the upper horn propagates toward the plasma critical surface and is reflected. Displayed here are contours of constant positive electric field, together with the more standard ray-tracing results. Note that the ray-trace trajectories are perpendicular to the wave fronts as the waves move away from the plasma. Near the critical surface, a very complex field structure exists, consisting of both standing and propagating waves. Unlike the 1D case, in which incident and reflected waves must have equal amplitudes, the geometric fall off of the fields, together with the curved geometry of the critical surface result in a very rich field pattern, and corresponding plasma current distribution. Even well away from the critical surface, interference effects are evident, as are diffraction effects near the horns. Finally, note that the waves propagate smoothly off the grid as a result of the radiative boundary conditions.

4. Density Pulse Propagation

In a manner similar to that explored by Cripwell (Cripwell, 1992) for a 1D code, we now launch a Gaussian density pulse propagating outward from the center of the plasma. The density profile with the perturbation may be described as

$$\frac{\omega_p^2}{\omega^2} = \frac{\omega_{p_o}^2}{\omega^2} \left[1 + a_f \exp \left(-\frac{(x - x_f)^2}{w_f^2} \right) \right] \quad (8)$$

where x_f and w_f are the x position and $1/e$ half-width of the pulse, respectively, and a_f is the fluctuation amplitude. The pulse moves at constant velocity from $x_f = 16\lambda_o$ to $x_f = 0$ during the run. Figure (2) shows the amplitude and phase as a function of time in the receiver waveguide for two pulse amplitudes; $a_f = 0.01$, and 0.10 , with $w_f = \lambda_o/2$. The temporal position of the peak phase change in both cases matches well with the location of the pulse, once the group delay from the critical surface is considered. The phase changes very quickly as the pulse arrives from the high density side of the critical surface, but then decays slowly as the pulse moves away, since the pulse is now continuously in the beam path. Each of the ripples evident on both the amplitude and phase occurs as the pulse moves an incremental distance $.5\lambda_o \leq \Delta x \leq \lambda_o$, and is the result of interference between the waves scattering from the critical surface and the propagating density pulse. As will be discussed below, the angular response of the waveguide tends to enhance this effect. A comparison of the 0.01 and 0.10 fluctuation amplitude cases indicate that the peak amplitude and phase response are linear functions of the pulse amplitude. Finally, note that even the relatively small density perturbations modelled here result in large changes in signal amplitude. Much higher edge-plasma fluctuation levels are found during many tokamak discharges.

In Figure (3) we again show the data from Figure (2) but with an expanded time scale. We also plot the signals detected $4\lambda_o$ above the midplane, together with 1D full-wave results calculated by the method of Hutchinson (1992). The 1D result has been time-shifted by the group delay to the critical surface. The peak phase response agrees well in all cases. However, the waveguide results show rapid variations in both amplitude and phase. Since the waveguide and horn modelling the reflectometer receiver will produce both amplitude and phase variations as a function of entrance angle to the horn, we would expect some additional variation as the fluctuations modify the reflected wave trajectories. It should also be pointed out that the transmitting horn is above the midplane, which together with the curved density contours, causes stronger signals to be reflected above the midplane. Therefore, signals detected above the midplane also tend to be less affected by “spurious” signals produced by diffraction off the edges of the horns.

5. Radially Propagating Oscillatory Modes

We now investigate the propagation of radial oscillatory modes in the plasma ($k_\theta = 0$, $k_r \neq 0$). For this case, we allow density waves to propagate in the $-x$ direction with no variation in the y direction. The density profile is described by

$$\frac{\omega_p^2}{\omega^2} = \frac{\omega_{p_o}^2}{\omega^2} \left[1 + a_f \sin \left(\frac{2\pi}{\lambda_f} x + \omega_f t \right) \right] \quad (9)$$

where λ_f and ω_f determine the fluctuation wavelength and frequency respectively. In Figure (4), we set $a_f = 0.01$ and plot the change in amplitude and phase of the echo signal as a function of fluctuation wavelength normalized to the vacuum wavelength. We show several cases, including results measured in the waveguide and at $y = 4\lambda_o$. In all cases, for

$\lambda_f \simeq \lambda_o/2$ there is very little response, as has been previously noted in 1D full-wave results (Zou, 1991, Hutchinson, 1992, Bretz, 1992). The fluctuation wavelength in this case is much shorter than the field wavelength at the critical surface, and the perturbed current distribution does not effectively radiate. As the fluctuation wavelength is increased beyond $\lambda_o/2$, however, the Bragg condition will be satisfied and the response away from the critical surface will be enhanced (Zou, 1990, Mazzucato, 1990, Zou, 1991, Hutchinson, 1992, Bretz, 1992). It should be pointed out that the measured phase response is in fact the interference between echo signals reflected from the critical surface and back-scattered signals off fluctuations from the region in which the Bragg condition is satisfied. Thus a decrease in the amplitude of the echo signal from the critical surface can enhance the phase response caused by the fluctuations.

The amplitude and phase response in Figure (4) will eventually saturate for long fluctuation wavelengths since the fluctuations begin to look more and more like a simple scaling of the entire density profile which both modulates the optical pathlength and moves the critical surface. Note that the waveguide results are well off the 1D full-wave curve, while the above-midplane results show good agreement. As in the pulse propagation case, the fluctuations modify how the waves propagate into the horn and waveguide, and hence the detected phase and amplitude. The above midplane results, on the other hand, agree with the 1D full-wave results to within 10%. In general, above-midplane agreement with 1D results improves as one moves the horns further from the detector, and waves diffracted from the horns no longer interfere as strongly with those scattered directly from the plasma. Finally, one should not assume from the data shown that the 2D full-wave phase response is always systematically higher than one would expect from 1D analysis. In fact, the 2D

results are very sensitive to the transmitting and receiving horn geometry, and can be well above or below the 1D result. The agreement should improve in cases where the critical surface is many wavelengths from the horns, and all waves enter the receiving horn at small angles.

The degree to which scattering away from the critical surface occurs will play a large part in determining how well the reflectometer measurements can be localized. We should note that in the 1D case, in a lossless medium, localization is enhanced by the swelling of the electric field near the critical surface, which results in larger scattered fields there. On the other hand, in the 2D case, the fields are much more likely to drop off as one approaches the critical surface because of geometric effects and refraction. Thus we might expect scattering away from the critical surface to play more of a role in a 2D simulation and indeed in the actual experiments. Also, scattering away from the critical surface will necessarily occur closer to the receiver and will thus be stronger than a similar signal propagating from the critical surface. At least one 1D code has modelled some of these effects with the inclusion of absorption in the dielectric term, so that the waves are attenuated as they propagate (Hutchinson, 1992).

In order to make some attempt at gauging the localization of the radial modes, we propagate Gaussian wave packets radially outward from the center of the plasma, with $a_f = 0.01$, and a $1/e$ full-width of $2\lambda_o$. The density is given by

$$\frac{\omega_p^2}{\omega^2} = \frac{\omega_{p_o}^2}{\omega^2} \left[1 + a_f \sin(k_f(x - x_f)) \exp\left(-\frac{(x - x_f)^2}{w_f^2}\right) \right] \quad (10)$$

where, as in the pulse propagation case, we allow the packet to propagate from $x_f = 16\lambda_o$ to $x_f = 0$. In Figure (5) the signal amplitude, phase,

and density perturbation at the critical surface as a function of time are shown. Figs (5a)–(5c) show results with $\lambda_f = \lambda_o$, while in Figs (5d)–(5f), $\lambda_f = 0.75\lambda_o$. Note, first of all, that in the long wavelength case both the amplitude and phase correlate well with the perturbations. However, for the short wavelength case, we see that both amplitude and phase can be more complicated, with more temporally extended oscillations. The pulse in both cases propagates a distance of λ_o in a time of $67\tau_o$. The Bragg condition is met in the long wavelength case at a distance λ_o past the critical surface, and for the short wavelength case, a distance $2\lambda_o$ past the critical surface (see Figure 6). Thus the packet passes the $\lambda_f/\lambda_o = 1$ surface $67\tau_o$ after the critical surface while the $\lambda_f/\lambda_o = 0.75$ surface is passed at $134\tau_o$. If we now include the propagation time from the two surfaces of $12\tau_o$ and $10\tau_o$, we would expect to see the signals from the two surfaces arrive at $79\tau_o$ and $144\tau_o$. In fact, if we do cross-correlations of the phase and amplitude with the perturbation in Figs (5a)–(5c), we find lag times of $83\tau_o$ and $87\tau_o$, respectively. Using the data from Figs (5d)–(5f), we find $138\tau_o$ and $141\tau_o$ for the phase and amplitude lag times. Thus, for both the short and long fluctuation wavelength cases, we find that the maximum response is occurring after the fluctuation has passed the critical surface, at a point close to where we would expect the Bragg condition to be met. However, the degree to which the echo signal generated by the packets correlates with the packet wave shape depends on the packet wavelength. Referring to Figure (6b), the long wavelength fluctuation which is phase matched in a region with a short matching condition scale-length generates a well correlated echo signal. The short wavelength fluctuation, phase matched in a longer scale-length region, continues to produce an echo signal as it propagates well past the phase matching region.

6. Poloidally Propagating Oscillatory Modes

To model poloidally propagating modes, we sinusoidally modulate the density profile in the y direction ($k_\theta \neq 0$, $k_r = 0$). As the mode propagates, it remains centered at x_f with a $1/e$ Gaussian width of w_f . The density profile is described by

$$\frac{\omega_p^2}{\omega^2} = \frac{\omega_{p_o}^2}{\omega^2} \left[1 + a_f \sin \left(\frac{2\pi}{\lambda_f} y + \omega_f t \right) \exp \left(-\frac{(x - x_f)^2}{w_f^2} \right) \right] \quad (11)$$

where ω_f is the fluctuation frequency. In Figure (7), we show the amplitude and phase of the detected signal as a function of time for several fluctuation wavelengths, with $w_f = .5\lambda_o$, $a_f = 0.10$, and $x_f = 10.75\lambda_o$ ($0.5\lambda_o$ in front of the critical surface). The response to the fluctuations is very strong for the $\lambda_f = 4\lambda_o$ case, but drops off very rapidly as the wavelength decreases. There is very little response for the $\lambda_f = \lambda_o$ case; a case for which the fluctuation wavelength is shorter than the local field wavelength (see again Figure 6). Note that for $\lambda_f = 4\lambda_o$, the signal amplitude is actually reduced to zero as the mode propagates. Also note that the signal can be enhanced by almost a factor of three over the no fluctuation level as the mode rotates, and the return beam is scanned across the receiving horn. These effects represent a complex combination of Doppler shifted return signals from the moving fluctuations and simple changes in the beam propagation trajectory. Phase changes of approximately $\pm\pi$ occur when the signal amplitude approaches zero. Such phase and amplitude changes result when not one but at least two waves of similar amplitude interact in the receiver. Since a minimum in the total signal occurs when the two signals are out of phase, we would expect to see jumps of $\pm\pi$ in the phase as their relative amplitudes change. Such phase changes have been seen in at least one experiment (Hanson, 1990, 1992). We

would also expect the amplitude to increase up to a factor of four when they are in phase. Using a rotating grating as an analogue, one has both O^{th} and 1^{st} order components in the received signal. The 1^{st} order component is Doppler shifted relative to that of the O^{th} order. For such a scenario, one would also expect the O^{th} order component to be more localized to the midplane than the 1^{st} order one. As one moves away from the midplane, the Doppler shifted component will become more dominant and the phase of the signal detected should begin to ramp. In Figure (8), for $a_f = 0.10$, $\lambda_f = 3\lambda_0$, and $w_f = 2\lambda_0$, the amplitude and phase of just such a signal are shown. It should be pointed out that the amplitude does not have to go to zero to generate this effect. The requirement is just that the 1^{st} order component be larger than the O^{th} order one. In actual experiments, misalignment of the horns or movement of the plasma off the midplane could result in such a situation. We should also mention that, since only a few fluctuation periods are illuminated in this example, the grating modelled here is a very low resolution, inefficient one, and the primary effect at the receiving horn results from shifts in alignment.

In Figure (9) we again address the issue of localization. Here we have plotted the amplitude and phase response to a poloidally propagating mode as a function of distance from the critical surface for two fluctuation wavelengths of $4\lambda_0$ and $2\lambda_0$. The radial width of the fluctuation in both cases was λ_0 and the fluctuation amplitude was 0.10. Note that in both cases very large amplitude variations occur, even well away from the critical surface. For the long wavelength case in particular, we see much larger phase changes near the critical surface than one would predict from a 1D full-wave analysis (solid line) of a Gaussian shaped density pulse the same width and amplitude as the poloidal fluctuation. On the other hand, the 1D full-wave phase response becomes larger than the 2D code

result as one moves away from the critical surface, since the 2D code response is a spatial average over a large fraction of a fluctuation wavelength. In fact, as the fluctuation wavelength is decreased, the response will tend to zero, so that in the short wavelength case, the 1D full-wave response is larger for all fluctuation locations. The fluctuation located at $0.5\lambda_o$ has, in fact, caused a complete loss of signal, and in an actual experiment would have resulted in “lost” fringes. As was discussed earlier, these very large effects are primarily caused by changes in the beam propagation trajectory near the critical surface. Thus, the fluctuation response will be well localized to the critical surface, but directly relating a fluctuation amplitude to a measured phase response will be very difficult. This effect taken together with the fact that the response is highly wavelength dependent, implies that one must take great care in drawing any conclusions from the phase response. Note that the 2D phase response peaks at the same location in both the short and long wavelength cases, approximately $.5\lambda_o$ in front of the critical surface. Zou (1990) has shown analytically that the selection rules governing 2D scattering of plane waves off of poloidal fluctuations should result in a movement of the peak phase response away from the critical surface. However, the complexity of the geometry modelled here makes quantitative comparisons difficult. Also, we should note that a case with $\lambda_f \leq \lambda_o$ might have shown more of an effect, since the matching conditions would have applied farther from the critical surface.

Finally, in Figs (10) and (11) we show contour plots of the electric field for fluctuations with two different “poloidal mode-numbers” and density scale-lengths. In Figure (10), we show a very long wavelength case in which the fluctuations result mainly in the return beam scanning over the receiving horn as the fluctuation propagates. We show a point

in time at which a minimum in the the fluctuation is centered near the source horn, and the return beam has been made to diverge away from the midplane. At other times during a fluctuation period, the return beam can be made to converge on the midplane or scan above or below it. In Figure (11), with a shorter fluctuation wavelength, and shorter density scale-length, we see that the return power is beginning to develop a mode structure reminiscent of an uncollimated reflection from a grating. The mode structure in this case does not change significantly during a fluctuation period.

7. Summary

We have tried to highlight in this paper some of the interesting fluctuation induced effects possible in a reflectometry experiment. Both radially and poloidally propagating modes can induce very large changes in amplitude and phase in the echo signal, even at fairly low fluctuation amplitudes. Not only do fluctuations affect the signal by changing the propagation path, they also result in Doppler shifted return signals that can interfere with the unshifted signal from the critical surface. One would think from these results that limiting the receiver bandwidth to some fraction of the fluctuation frequency would improve the density profile measurements, and this has been shown to be the case experimentally (Prentice, 1988). In addition, scattering away from the critical surface can become very important as the fluctuation amplitude is increased or the density profile broadened. This effect limits the localization one can expect in the detection of radially propagating oscillatory modes. This result is consistent with earlier 1D results, though the 2D geometry admits far more complex solutions. Refraction of the waves by the plasma, and the natural fall off of the fields with distance from the source, will

enhance this effect. The 2D code results indicate that the response to poloidal modes can be well localized near the critical surface, but a complete scan of phase response vs. fluctuation wavelength has not yet been carried out. An enhanced response away from the critical surface may well also occur for poloidal modes. We have shown that phase ramping of the return signal can result from the propagation of poloidal fluctuations near the critical surface.

Certainly much more complex wave structures exist in tokamaks than those modelled in this paper. For example, drift wave turbulence is probably responsible for much of the amplitude and phase change seen in reflectometry data from tokamaks. However, as we have shown here, even the coherent mode results are not straightforward and easy to understand. Still, some attempt at modelling these modes should eventually be made.

Finally, it is important to point out that direct comparison with experimental results has not yet been attempted, but is very much needed to limit the parameter space over which the code is run. Large changes in signal level and phase can be obtained by making small changes in fluctuation scale-length, level, and location. Likewise, small changes in density profiles together with the experimental geometry can result in dramatic changes in the return signals. In the near future, the code will be used to model results from the C-Mod Narrow-Band Reflectometer (Stek, 1990).

Acknowledgements

The authors wish to thank Stephen Wolfe for many discussions along the way, and for his critical analysis of this paper. It is with great appreciation that we thank Miklos Porkolab for asking some very good questions about the Versator II reflectometry experimental data. We would also like

to thank Terry Rhodes for several fruitful conversations concerning his experimental data, and Paul Bonoli for advice on various numerical techniques. This work was supported by the U.S. Department of Energy contract No. DE-AC02-78ET5103.

References

- BLASCHAK J.G., KRIEGSMANN A.K. (1987) *J. Comput. Phys.* **77**, 109.
- BOTTOLLIER-CURTET H., and ICHTCHENKO G. (1986) *Rev. Scient. Instrum.* **58**, 539.
- BRETZ N. (1992) *Phys. Fluids B* **4**, 2114.
- BULANIN V.V. (1992) Proceedings of the IAEA Technical Committee Meeting on Microwave Reflectometry for Fusion Plasma Diagnostics, England.
- COSTLEY A.E., CRIPWELL P., PRENTICE R. and SIPS A.C.C. (1990) *Rev. Scient. Instrum.* **61**, 2823.
- CRIPWELL P., COSTLEY A.E. and HUBBARD A.E. (1989) *Proc. 16th European Conf. on Controlled Fusion and Plasma Physics*, Venice, Italy, Vol. 13B, p. 75.
- CRIPWELL P. (1992) Proceedings of the IAEA Technical Committee Meeting on Microwave Reflectometry for Fusion Plasma Diagnostics, England.
- DOYLE E.J., LEHECKA T., LUHMANN N.C.Jr., PEEBLES W.A., PHILIPONA R., BURRELL K.H., GROEBNER R.J., MATSUMOTO H. and OSBORNE T.H. (1990) *Rev. Scient. Instrum.* **61**, 3016.
- GIVOLI D. (1991) *J. Comput. Phys.* **94**, 1.
- HANSON G.R., ANABITARTE E., BELL J.D., HARRIS J.H., THOMAS C.E., and WILGEN J.B. (1989) 31st Annual Meeting of the APS, Division of Plasma Physics.

- HANSON G.R., HARRIS J.H., BELL J.D., WILGEN J.B., AN-
 ABITARTE E., BRANAS B., DUNLAP J.L., HILDAGO C.,
 SANCHEZ J., THOMAS C.E., and UCKAN T. (1990) 32nd An-
 nual Meeting of the APS, Division of Plasma Physics.
- HANSON G.R., HARRIS J.H., WILGEN J.B., THOMAS C.E., ACETO
 S.C., BAYLOR L.R., BELL J.D., BRANAS B., DUNLAP A.C.,
 ENGLAND A.C., HIDALGO C., MURAKAMI M., RASMUSSEN
 D.A., SANCHEZ J., SCHWELBERGER J.G., UCKAN T., and
 ZIELINSKI J.J., (1992) *Nuc. Fusion* **32**, 1593.
- HIGDON R.L. (1986) *Math. Comput.* **47**, 437.
- HUBBARD A.E., COSTLEY A.E., and GOWERS C.W. (1987) *Journal
 of Physics E* **20**, 423.
- HUTCHINSON I.H. (1987) *Principles of Plasma Diagnostics*, Cambridge
 University Press, Cambridge.
- HUTCHINSON I.H. (1992) *Plasma Phys. and Contr. Fusion* **34**, 1225.
- IRBY J.H. and STEK P. (1990) *Rev. Scient. Instrum.* **61**, 3052.
- MAZZUCATO E. and NAZIKIAN R. (1991) *Plasma Phys. and Contr.
 Fusion* **33**, 261.
- MILLOT P., MOURGUES F., and PAUME M. (1990) 17th EPS Confer-
 ence, Amsterdam.
- PRENTICE R., CRIPWELL P., CLARKE H.E., COSTLEY A.E., FES-
 SEY J.A., HUBBARD A.E., HUGENHOLTZ C.A.J., OYEVAAR
 T., PAUME M., PUTTER A.J., SIPS A.C.C., and SLAVIN K.
 (1988) 30th Annual Meeting of the APS, Division of Plasma
 Physics.
- SANCHEZ J., ESTRADA T., and HARTFUSS H.J. (1992), Proceedings
 of the IAEA Technical Committee Meeting on Microwave Reflec-
 tometry for Fusion Plasma Diagnostics, England.

- SIMONET F. (1985) *Rev. Scient. Instrum.* **56**, 664.
- STEK P.C., and IRBY J.H., (1990) 32nd Annual Meeting of the APS,
Division of Plasma Physics.
- TFR Group (1985) *Plasma Phys. and Contr. Fusion* **27**, 1299.
- ZOU X.L., LAURENT L., LEHNER T. and RAX J.M. (1990) Localiza-
tion of Fluctuation Measurement by Wave Scattering Close to a
Cut Off Layer, 17th EPS Conference, Amsterdam.
- ZOU X.L., LAURENT L., and RAX J.M. (1991) *Plasma Phys. and
Contr. Fusion* **33**, 903.

Figure Captions

- Fig. 1 Contour plot of the positive half of the electric field with contour levels of 0.05, 0.1, 0.2, 0.4, 0.8, 1.6, and 3.2 V/m. The dotted lines radiating from the source waveguide are ray-trace trajectories. The solid lines on the right are contours of $\frac{\omega^2}{\omega_p^2} = 0.5, 1.0, \text{ and } 1.5$.
- Fig. 2 Time histories of the electric field amplitude (a), and electric field phase (b), are shown. Results with pulse amplitudes of 0.10 (solid), and 0.01 (dotted) are shown. The largest change in phase occurs in both cases when the pulse is located near the critical surface (when propagation time from the critical surface to the detector is allowed for). Note that the upper scale in each plot represents the pulse position relative to the critical surface at the midplane.
- Fig. 3 Expanded time scale version of Figure (2) showing the change in field amplitude (a), and phase (b). Results are shown for signals detected in the receiver waveguide (solid) and $4\lambda_o$ above the midplane (dotted), with $a_f = 0.10$. The waveguide signal shows more rapid amplitude and phase variation, but the peak amplitude and phase changes are very similar. Note also that the phase response is very similar to the 1D full-wave result (dot-dash). Waveguide results with a fluctuation amplitude of 0.01 are also shown (dashed).
- Fig. 4 Scaling of the change in electric field amplitude (a), and phase (b), are shown as a function of the fluctuation wavelength for radially propagating modes. Signals from the waveguide (*), and $4\lambda_o$ above the midplane (\diamond) are shown. The above-midplane results are a good match to the 1D full-wave result (solid line). 1D WKB results are also shown (dotted line) for comparison. above-midplane

results with the horns moved downward $0.40\lambda_o$ show very good agreement with the 1D full-wave results (Δ).

Fig. 5 Time histories of the electric field amplitude, phase, and packet density perturbation are shown for two values of λ_f/λ_o . $\lambda_f/\lambda_o = 1.0$ for (a)–(c), and $\lambda_f/\lambda_o = 0.75$ for (d)–(f). The delay in the phase and amplitude responses indicate that the Bragg matching condition is met in both cases. The upper scale in each plot represents the packet position relative to the critical surface at the midplane.

Fig. 6 Plot of $\frac{\omega_p^2}{\omega^2}$ (a), λ_f/λ_o required for meeting the Bragg condition (b), and the electric field (c), as a function of radial position along a horizontal line through the source. Note that the electric field drops off rapidly as you leave the source located at $x = \lambda_o$.

Fig. 7 Time histories of the electric field amplitude (a), and phase (b) in the presence of poloidally propagating modes with $a_f = 0.1$, and $\lambda_f/\lambda_o = 4.0$ (solid), 3.0 (dashed), 2.0 (dotted), and 1.0 (dot-dash). Phase shifts of approximately $\pm\pi$ occur near zeros in the signal amplitude. One complete fluctuation period is displayed.

Fig. 8 Time history of electric field amplitude and phase at points $4\lambda_o$ above (a,b), and $4\lambda_o$ below (c,d) the midplane. The phase continuously ramps in both cases, indicating the signal has a large Doppler shifted component relative to the source frequency. One complete fluctuation period is displayed. The curvature, κ , was 1000 for this example, which enhanced the 1st order return signal.

Fig. 9 Change in amplitude (a), and phase (b), as a function of poloidal mode position relative to the critical surface. Fluctuation wavelengths of $4.0\lambda_o$ (*) and $2.0\lambda_o$ (◇) were used, with a fluctuation amplitude of 0.10. The solid line represents the 1D full-wave solution

for a Gaussian pulse propagating through the same region. The dotted line is the 1D WKB result. The phase change in the $2\lambda_o$ case is displayed $\times 2$ for better comparison to the $4\lambda_o$ case.

Fig. 10 Contour plot of the electric field for a long wavelength fluctuation with $\kappa = 2.67$, and $\gamma = 1$. The main consequence of the fluctuation is that the return beam scans across the receiving horn as the fluctuation rotates.

Fig. 11 Contour plot of the electric field for a shorter wavelength fluctuation with $\kappa = 2.67$, and $\gamma = 2$. Now we see a more complex mode structure than seen in Figure (10), and O^{th} and 1^{st} order components begin to appear and overlap.

Figure 1

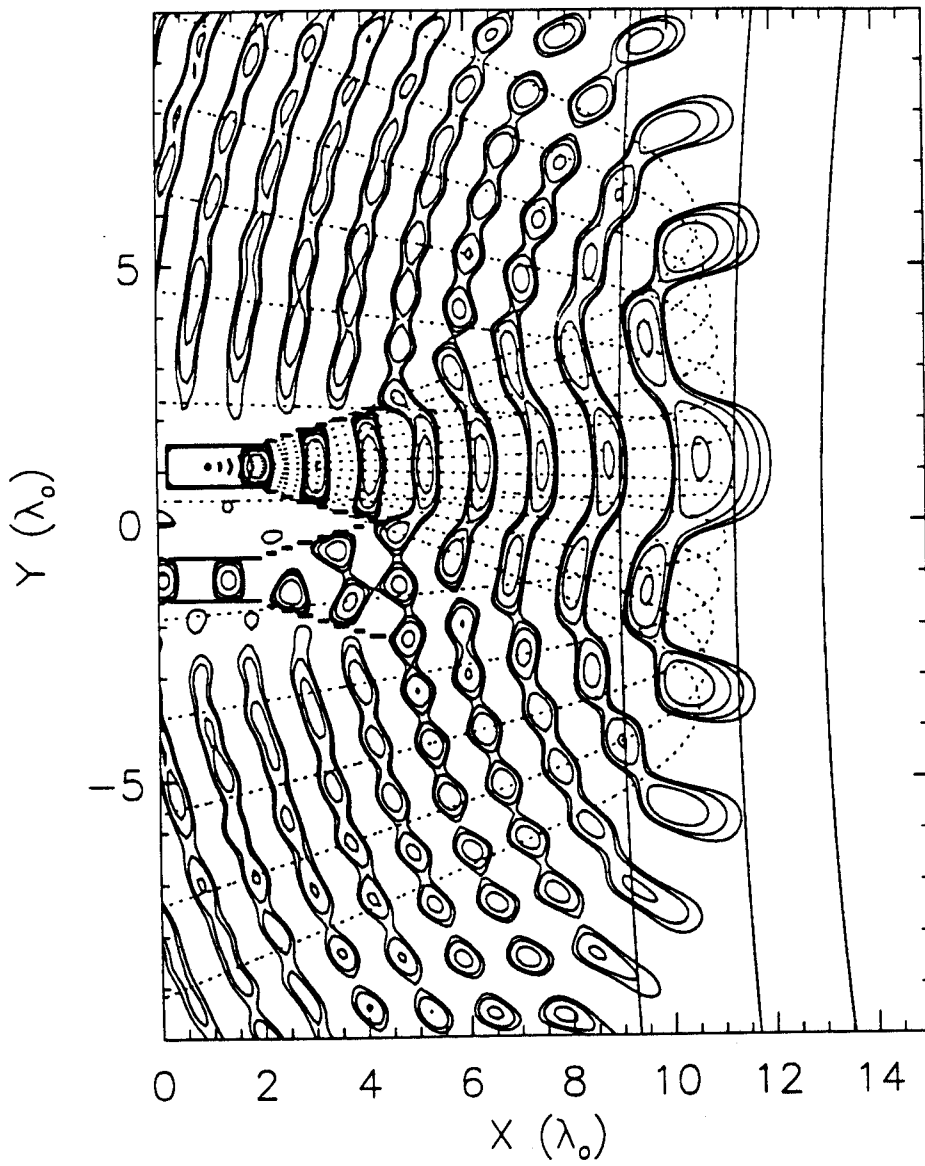


Figure 2

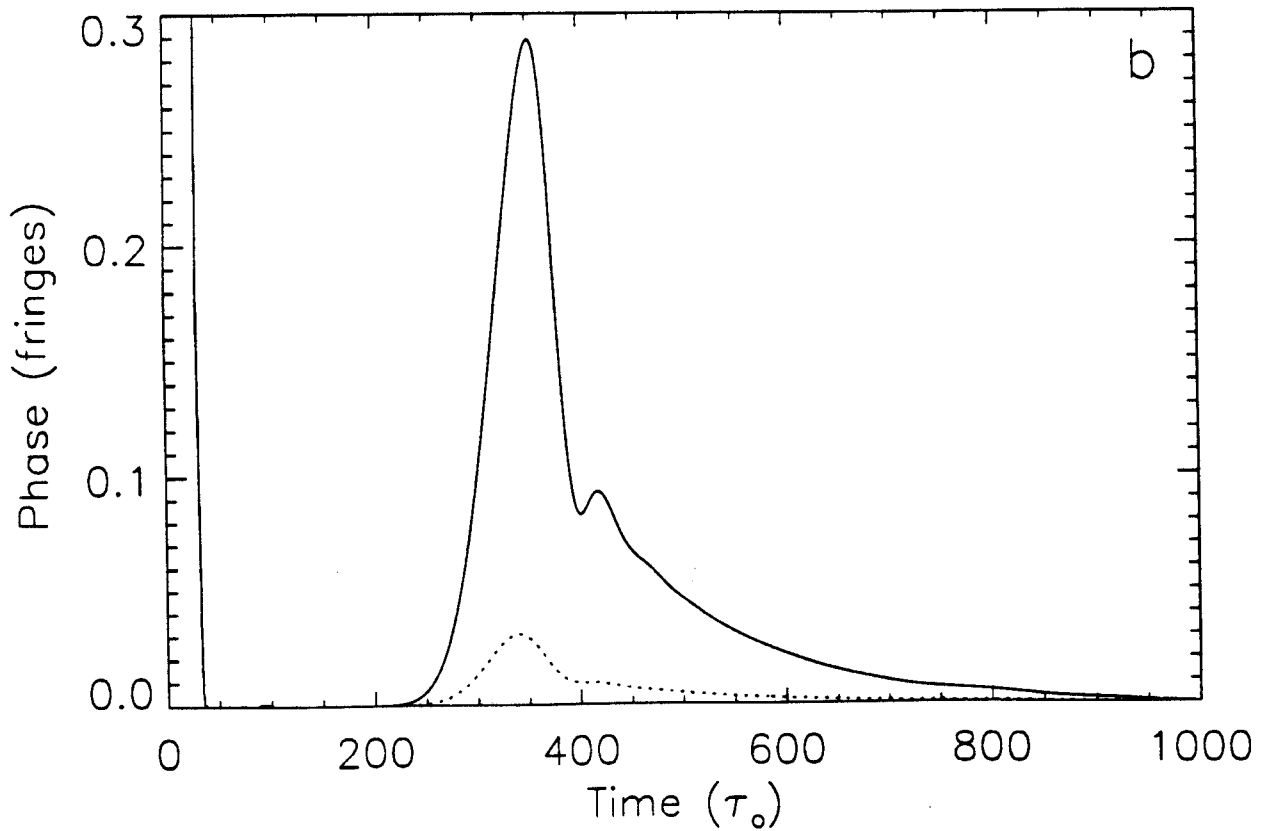
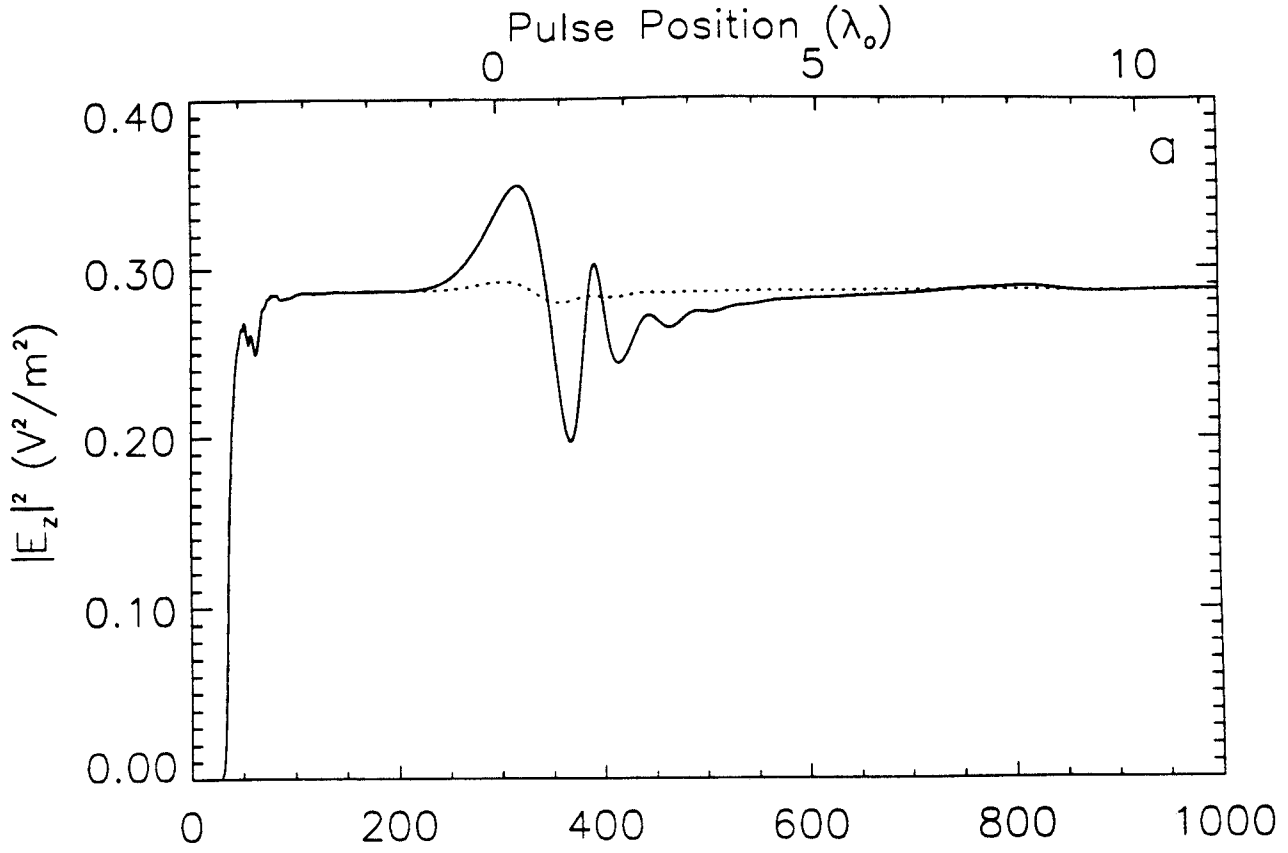


Figure 3

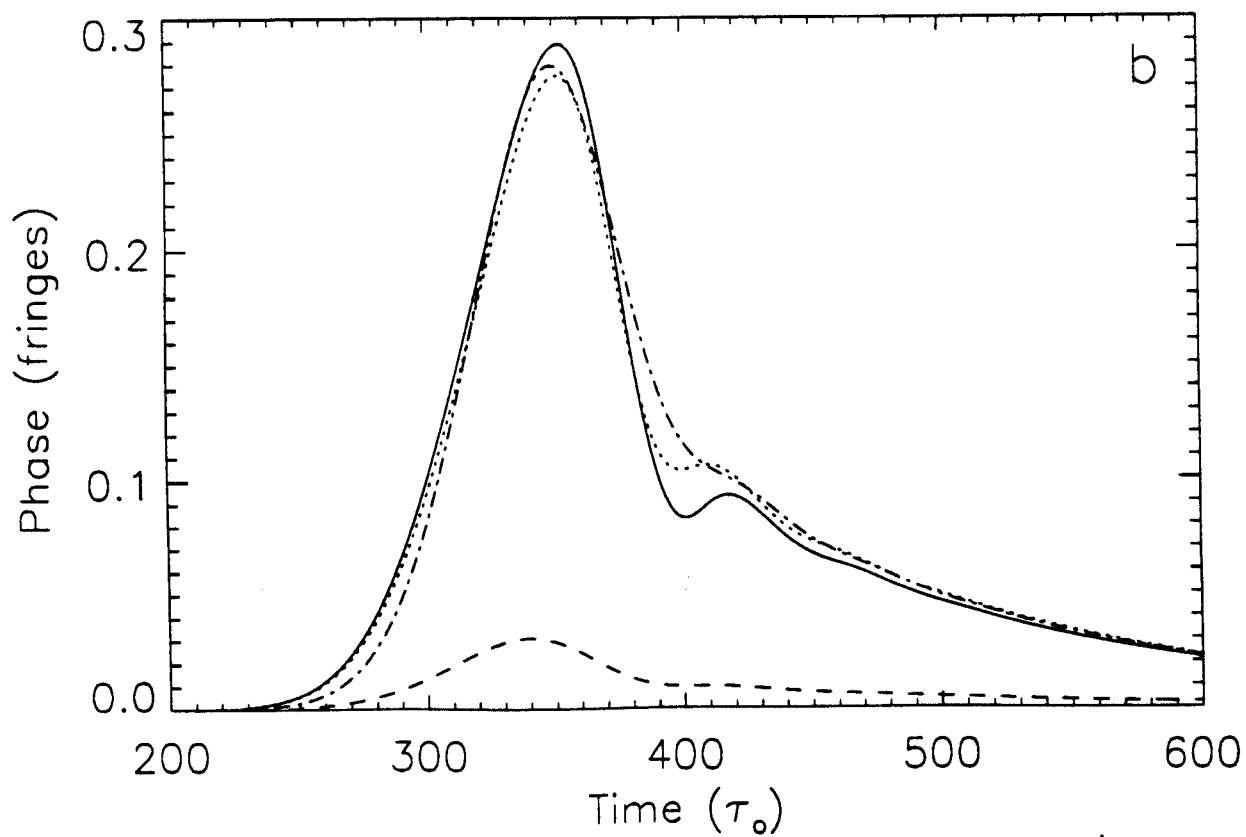
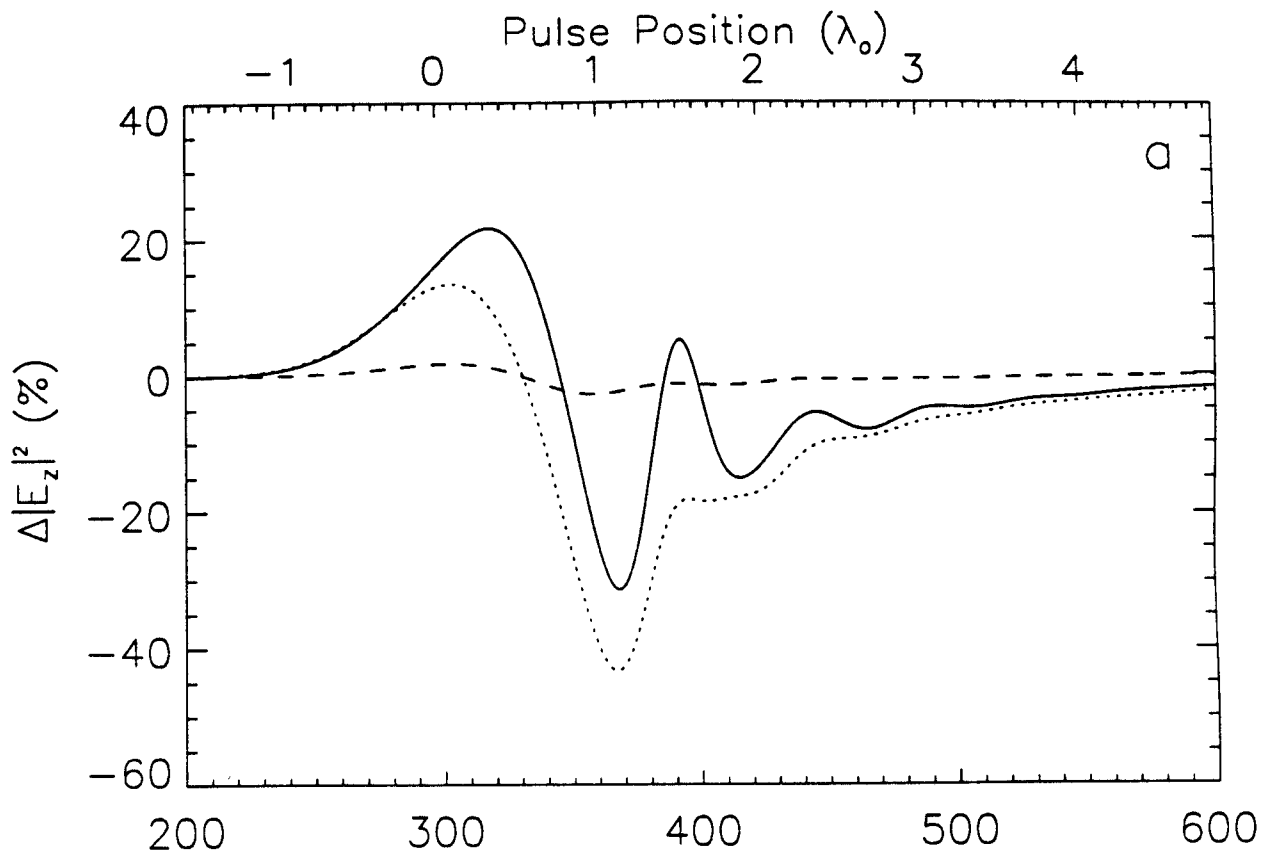


Figure 4

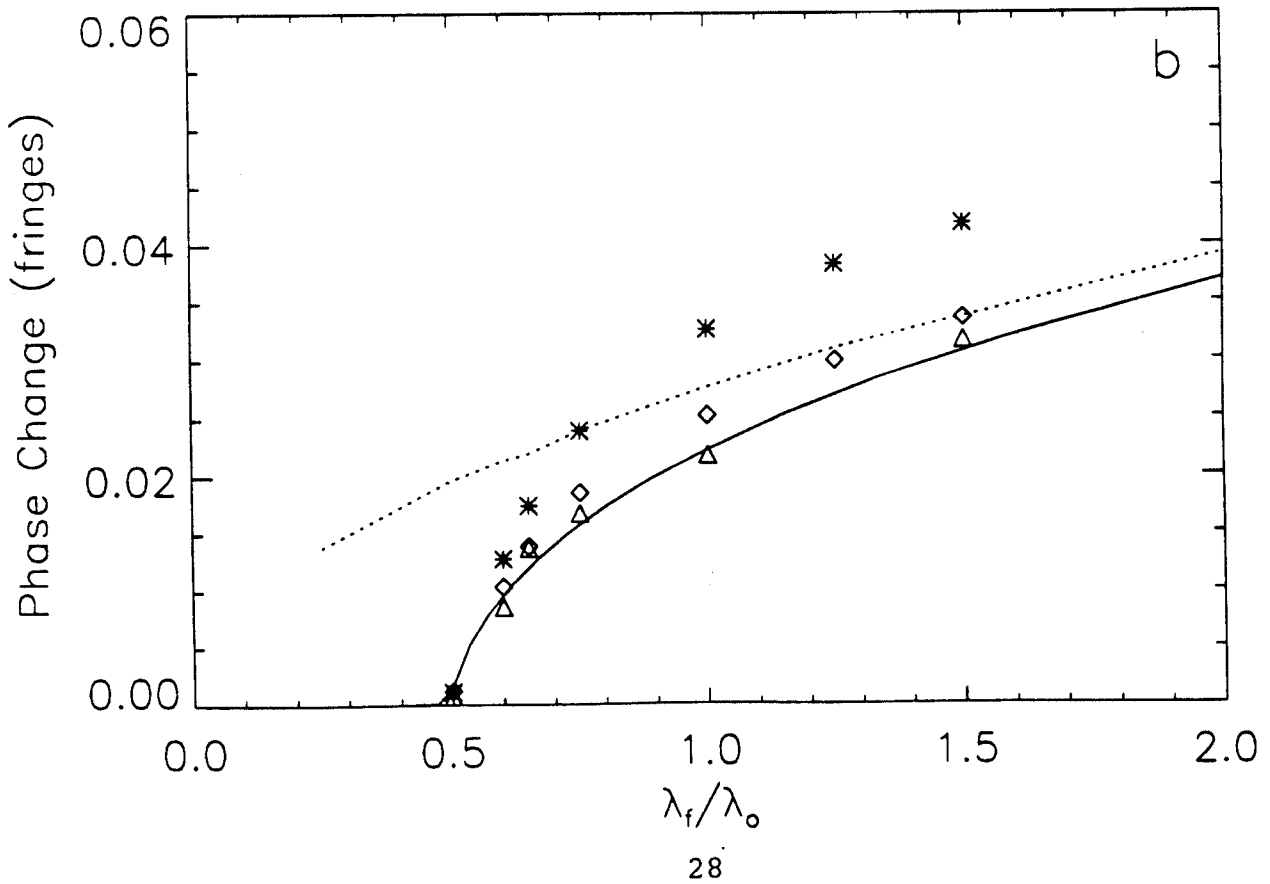
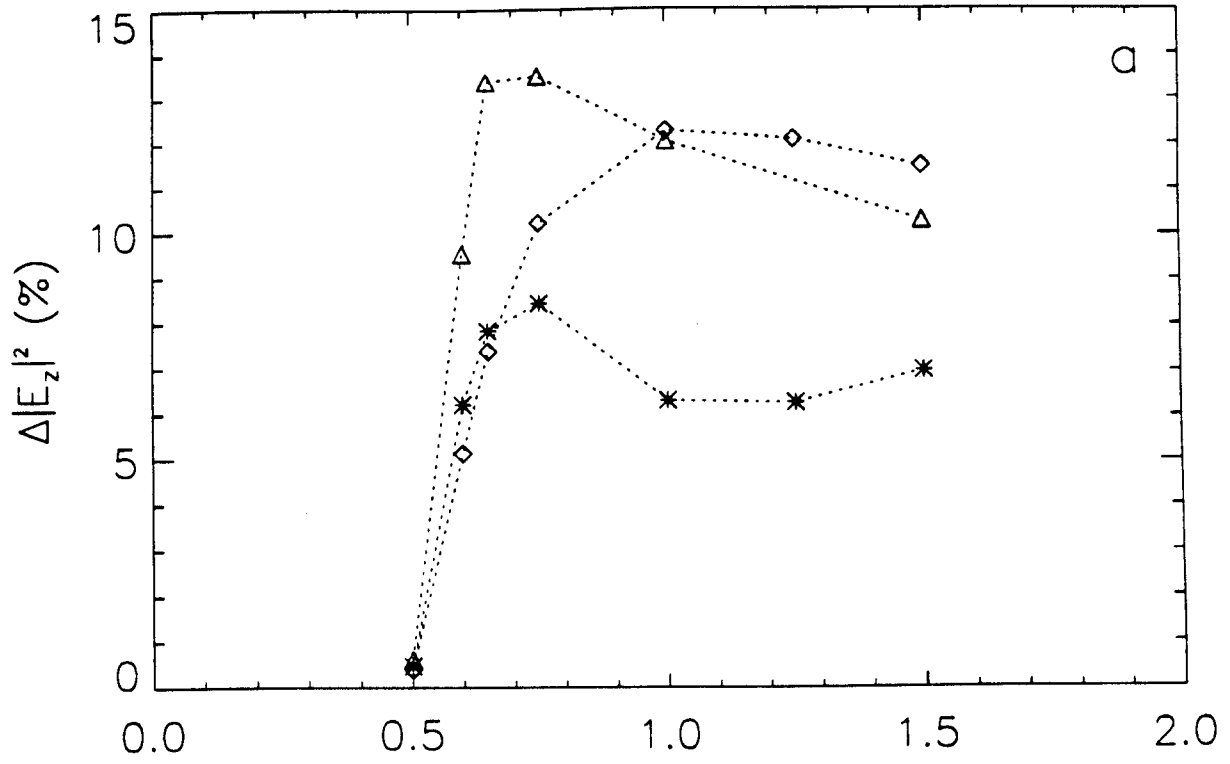


Figure 5

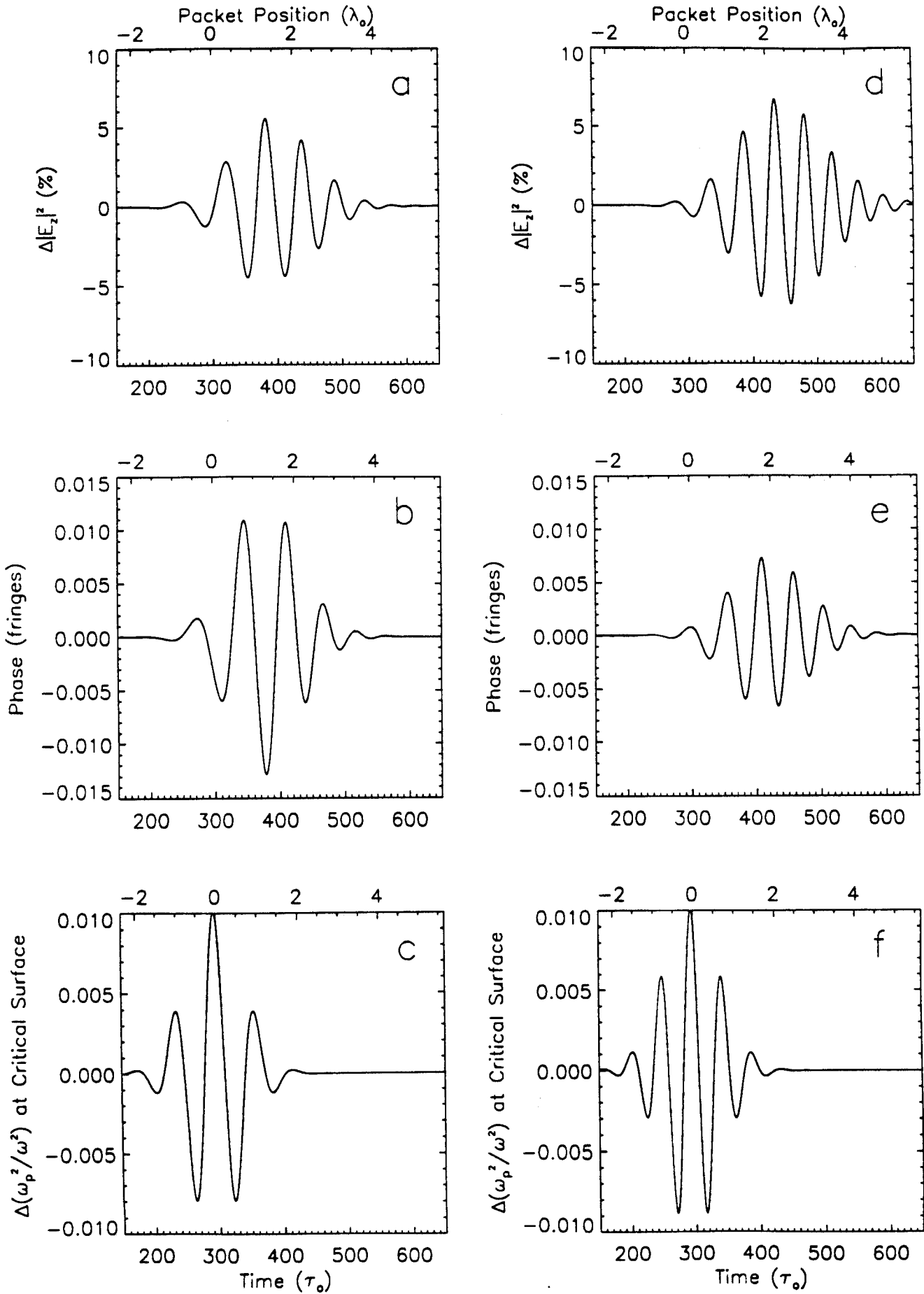


Figure 6

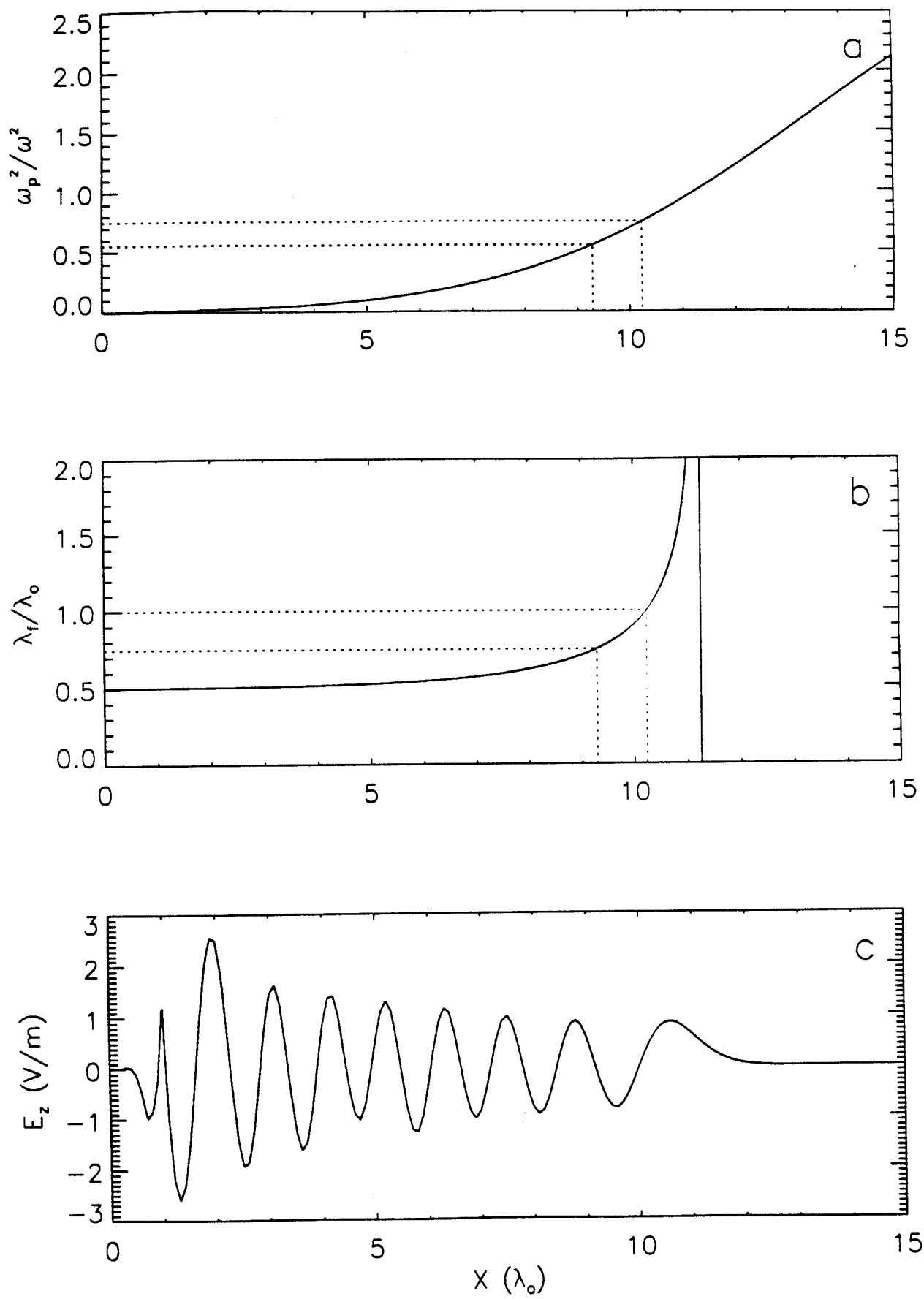


Figure 7

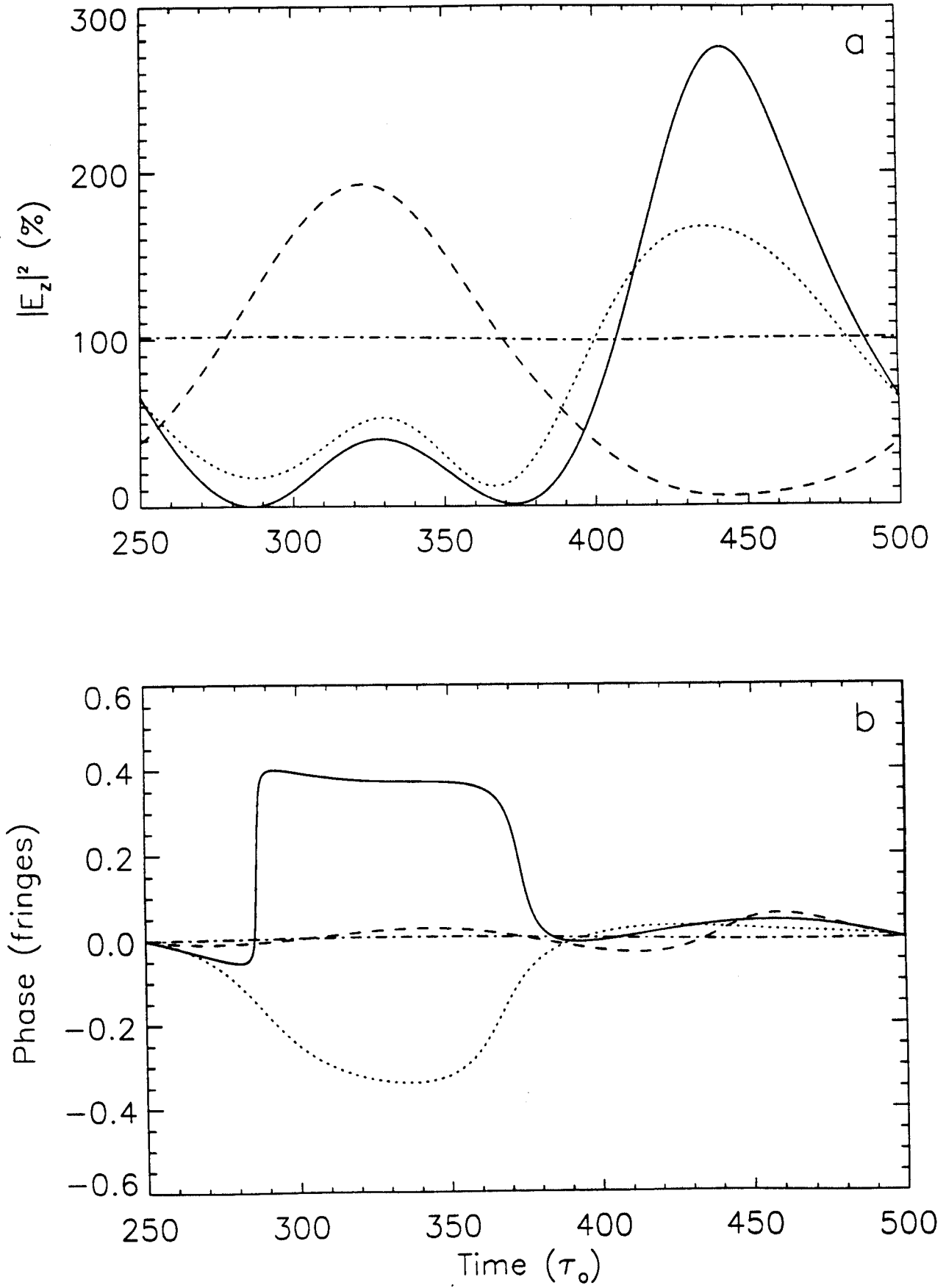


Figure 8

